Journal of Solar Energy Research (JSER)

Journal homepage: www.jser.ut.ac.ir

An Auxiliary Power System Based on Solar Photovoltaic for Enhanced Unmanned Aerial Vehicle Remote-Controlled Aircraft Endurance

Haura Haider Abdul Redha[a,*] Ahmed Hameed Reja[b], Ahmed Adnan Shandookh[c]

[a, b] *College of Electromechanical Engineering, University of Technology-Iraq, Al-Wehda neighborhood, Baghdad, Iraq.*
[c]*College of Mechanical Engineering, University of Technology-Iraq, Al-Wehda neighborhood, Baghdad, Iraq.*

ARTICLE INFO

Article Type:

Research Article

Received:2025.07.12
Accepted:2025.08.27

Keywords:
UAV; Solar - Power Augmentation; CFD ANSYS Fluent; Static Structural Analysis; EPP - Foam

A B S T R A C T

This research outlines the design, simulation, and structural evaluation of a solar-assisted power augmentation system integrated into an unmanned aerial vehicle (UAV) made of expanded polypropylene (EPP) foam. The system consists of two 1.5 W rigid monocrystalline solar panels mounted on the wings and an 18 W flexible panel mounted below the fuselage, which increased the UAV's weight from 170 g to 840 g. Aerodynamic performance was assessed using computational fluid dynamics (CFD) simulations in ANSYS Fluent over a sweep of angles of attack (–6° to 12°) at speeds of 10 m/s and 30 m/s. The results showed lift augmentation of over 300% with significant drag reduction. Structural simulations in ANSYS Mechanical using pressure loads from CFD results confirmed that the maximum principal stress and von Mises strain were kept within 70% of the material limits of the EPP foam. The most effective operating range was found to be between 3° and 9° AoA for low-speed flight and between 0° and 6° AoA for high-speed flight. This study confirms the feasibility of integrating monocrystalline solar modules into lightweight UAVs as a viable method of drastically extending flight endurance without sacrificing aerodynamic or structural integrity.

1. Introduction

Unmanned Aerial Vehicles (UAVs), especially remote-controlled (RC) fixed-wing platforms, have grown more and more sought after among numerous industries over the past few years due to their flexibility, minimal operating costs, and capacity to execute tasks ranging from precision farming, aerial mapping, and infrastructure inspections to surveillance and relief efforts in a disaster[1,2]. However, despite advancements in avionics, lightweight materials, and propulsion technologies, one age-old weakness continues to limit their range of operations: limited flight endurance. Almost all

*Corresponding Author Email: eme.23.113@grad.uotechnology.edu.iq

Cite this article: Abdul Redha, H. Haider, Reja, A. Hameed and Shandookh, A. Adnan (2025). An Auxiliary Power System Based on Solar Photovoltaic for Enhanced Unmanned Aerial Vehicle Remote-Controlled Aircraft Endurance. Journal of Solar Energy Research, 10(1), 2223-2233. doi: 10.22059/jser.2025.398475.1596

DOI: 10.22059/jser.2025.398475.1596

fixed-wing UAVs employ solely lithium batteries, providing a limited amount of energy that translates into quite short mission durations and frequent calls for recharging or battery replacement [3,4].

As missions in UAVs become more complicated and require extended coverage of broader geographical regions, onboard energy systems that are sustainable, autonomous, and efficient assume a prime significance[5]. Addressing this problem, solar photovoltaic (PV) technology presents huge potential [6]. Solar PV systems have the potential to harness solar radiation during flight, offering a renewable, light-weight, and committed power source that can complement the primary battery and enhance overall endurance[7–9].

The concept of integrating solar PV into a UAV is not novel, but its practical implementation has some drawbacks, such as achieving an optimum weight/power ratio, maintaining aerodynamic efficiency, and offering power management reliability. Successful integration demands a fine tuning of structure design, material selection, location of solar cells, and power electronics optimization such that the UAV is stable and maneuverable while deriving energy from the sun [10].

This study presents the development, simulation, and testing of an auxiliary power system from solar PV panels specifically for a fixed-wing RC plane. The system entails the tactical placement of light-weight solar panels with high efficiency on the wings and fuselage of the aircraft. A CAD model is outlined to identify mechanical compatibility and placement optimization for full solar exposure. Electrical modeling is performed in order to model actual-time energy generation under various conditions of irradiance. Aerodynamic and structural simulation is also performed to analyze how the integration of PV panels affects lift, drag, and structure.

The goal of this research is to fill that void by proposing and evaluating an auxiliary photovoltaic solar power system embedded in a radio-controlled aircraft made from expanded polypropylene (EPP) foam. A two-model simulation method is used.

1.Simulation of steady-state flow aerodynamics is done using ANSYS Fluent, where airflow is modeled at various angles of attack and flight speeds.

2.Structural analysis is performed using ANSYS Mechanical in order to find the stress distributions, strain concentrations, and material reactions under aerodynamic load conditions.

Recent studies have investigated different aspects of solar-powered UAV development. For instance, [11] presented a flight test of a solar UAV with integrated PV wings, while [12] demonstrated a multi-physics model combining aerodynamics, structure, and solar energy. However, most of these works analyzed individual aspects, either aerodynamic optimization or structural integrity, without presenting an integrated simulation framework. The present research fills this gap by combining CFD-based aerodynamic analysis with structural finite element simulations in one study, providing a holistic approach to evaluate solar-augmented UAV endurance and safety.

The findings of this study contribute to the design optimization of solar-augmented UAV systems, especially for small-scale or RC aircraft applications, where weight, endurance, and material safety are tightly constrained.

The novelty of this work lies in its integrated methodology that combines aerodynamic CFD simulations with structural FEA analysis under realistic loading conditions derived from CFD. Unlike previous studies that examined energy harvesting, aerodynamics, or structure separately, this research addresses all three aspects simultaneously. In addition, grid-independence testing, solution stability assessment, and validation with experimental data further strengthen the reliability of the findings. This integrated multi-physics approach has not been previously reported for small-scale RC UAVs with solar augmentation.

2. Materials and Methods

2.1. Proposed Methodology

Using a hybrid approach, this study looks at how fitting solar panels to an EPP/foam UAV wing changes its effectiveness during flight and its overall build. SolidWorks was used to model the basic form of the airframe (with a mass of 170 g) and the location of two 1.5 W/12 V solar panels on top and one 18 W/20 V flexible panel beneath. From what was built two models were taken out:

1.a simplified exterior meant for Reynolds-averaged Navier–Stokes calculations in ANSYS Fluent.

2. a fully-detailed shell and mount model for finite-element stress analysis in ANSYS Mechanical.

Separating the fluid from the structural approach, allowed for the optimal generation of meshes and convergence of solve results for both.

The core of the methodology is illustrated in Figure 1.

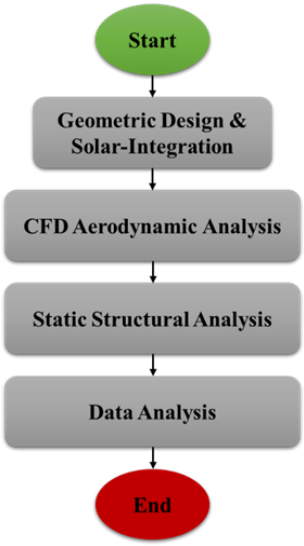

Figure 1. Proposed Methodology

From figure 1 comprises four sequential phases:
1.Geometric Design & Solar-Integration, wherein the CAD models are parameterized to reflect the exact dimensions, material properties, and mounting arrangements;
2.CFD Aerodynamic Analysis, which employs a C-type computational domain (inlet: 5× wingspan; outlet: 10×; lateral/vertical: 5×) and k–ω SST turbulence closure to simulate seven angles of attack (–6°, 0°, 3°, -3°, 6°, 9°, 12°) at two flight speeds (10 m/s and 30 m/s), extracting drag (F_D) and lift (F_L) forces and their vector components;
3.Static Structural Analysis, where the lift and drag vectors are converted into distributed pressure loads over defined reference areas (A_D = 0.175 m², A_L = 0.1457 m²) and applied to the detailed foam-EPP/solar-panel assembly under fixed-route constraints;
4.Data Analysis, which synthesizes aerodynamic coefficients, stress fields, and strain distributions into comparative plots and tables to determine safe operating envelopes and optimal angles for extended flight time.
With the steps settled, the study directly matches aerodynamic changes with responses from the structure, providing a reliable assessment of the impact of adding solar mass to the UAV's performance.

It should be noted that the two-model approach, separating CFD and structural analyses, was adopted to optimize meshing and reduce computational cost. However, this simplification does not fully capture the dynamic interaction between fluid flow and structural deformation. A coupled fluid–structure interaction (FSI) analysis would provide higher fidelity and is recommended for future research.

To strengthen the scientific foundation of the adopted numerical model, the governing equations of incompressible turbulent flow were considered. The Reynolds-averaged Navier–Stokes equations coupled with the k–ω SST turbulence model was solved to capture boundary layer separation and adverse pressure gradients with high accuracy. The use of ANSYS Fluent was motivated by its proven robustness in similar solar-aided UAV aerodynamic simulations reported in recent literature. In parallel, the static structural analysis was formulated using finite element methods based on linear elasticity theory, which allowed direct coupling of CFD-generated aerodynamic loads into the FEA structural domain. This dual theoretical–numerical framework ensures that the study is not purely simulation-based but also supported by physical and mathematical fundamentals, enhancing the scientific depth of the work.

2.2. Molding Design

2.2.1. Geometric Design and Solar- Integration

This part of the study deals with the engineering design of the drone and the solar integration strategy adopted to enhance its functionality and durability in long-term missions. A three-dimensional model was developed using CAD software to represent the entire structure of the aircraft along with the installed solar panels, which made it possible to accurately visualize the overall configuration and mass distribution.

2.2.1.1 CAD Model Development

Initially, a fully detailed 3D CAD model in SolidWorks® was made to show the airframe and the solar panel design together as show in figure 2. The structure of the airframe was built using EPP foam, resulting in a bare- aircraft mass of 170 g. Wingspan, mean aerodynamic chord, fuselage length and empennage measurements were established according to the goals outlined in the design brief so the vehicle would be aerodynamically realistic. Mounted on top of the wing are two broad acrylic solar panels rated at 1.5 W/12 V each and one flexible monocrystalline panel (420 × 280 mm, 18 W/20 V) was located under the fuselage. Accurate placement and removal of mass by flow surfaces was achieved

by building bespoke brackets and adding them to the wing and fuselage through parametric modeling.

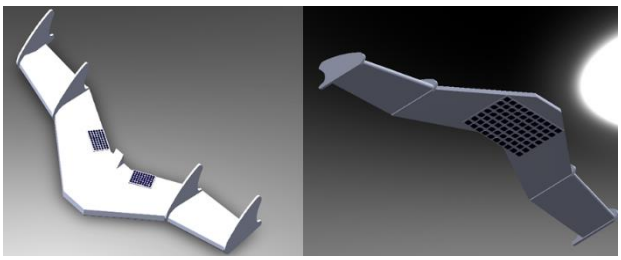

Figure 2. CAD model in SolidWorks

2.2.1.2 Model Variants for Simulation

In this segment two separate engineering models were developed to meet the requirements of fluid dynamics simulation and structural analysis of the aircraft using SolidWorks as show in figure 3.

The Computational Fluid Dynamics (CFD) model focuses only on the outer shell of the aircraft and solar panels, where internal components such as stabilizers, connectors, and electronics have been excluded, in order to facilitate grid generation and reduce computing power requirements.

As for the structural model, it is designed to include all the exact engineering details, including solar panel mounts, electronic component housings, and supporting elements, which allows ANSYS Mechanical to conduct accurate analyzes of stresses and strains caused by mechanical loads.

The simulations were carried out using numerical grids and separate physical settings for each model, which contributed to improving the accuracy of the numerical representation of the aerodynamic behavior and structural interactions of the aircraft, thereby reaching more reliable and efficient results in the design evaluation.

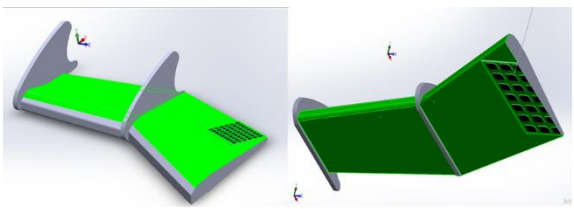

Figure 3. Second Model for Structural analysis showing area of wings

2.2.2 CFD Aerodynamic Analysis

In this part, the effect of integrating solar panels on the aerodynamic performance of the drone was evaluated by conducting advanced computational fluid dynamics (CFD) simulations. This analysis helped to predict the aerodynamic forces acting on the aircraft, in particular the lift and drag forces, under various flight conditions.

2.2.2.1 Computational Domain and Meshing

To model the airflow exactly, a C-type computational domain was developed for both the airplane and its panels as show in figure 4. A distance of five fuselage lengths was placed between each plane and the inlet plane position which was five times the fuselage length ahead of the nose (5 L). The lateral and vertical edges were drawn at five fuselage lengths (5 L) away from the aircraft centerline to reduce any disturbing or disruptive effects at the edges. In this domain, a core mesh in a tetrahedral shape was created and three prism layers were added to all boundaries to capture the boundary layer. The leading and trailing edges of the wing, as well as the areas around the solar- panel mounts and highly curved regions, were refined with finer mesh so that y^+ remained below 1, making it possible to observe the phenomena in the viscous sublayer precisely.

A grid-independence study was carried out to ensure that the obtained results were not sensitive to mesh density. Three grid configurations were tested: coarse (0.75 million cells), medium (1.20 million cells), and fine (2.00 million cells). The lift and drag coefficients obtained from the medium and fine meshes showed less than 2% variation, which confirmed that the solution is mesh-independent. Based on this outcome, the medium mesh was selected for all subsequent analyses as it provides a good balance between computational accuracy and efficiency.

Table 1 presents the results of the grid-independence study, showing that the variation in lift and drag coefficients between medium and fine meshes was less than 2%, which confirms mesh independence.

Table 1. Grid-Independence Study

Mesh Type	No. of Cells	CL	CD	Variation vs. Fine Mesh (%)
Coarse	0.75 M	0.642	0.037	5.8%
Medium	1.20 M	0.658	0.036	1.5%
Fine	2.00 M	0.668	0.036	–

Source: Authors' CFD simulation results.

Figure 4 shows the convergence of the lift coefficient (CL) with increasing mesh refinement, confirming that the medium mesh provides accurate results with acceptable computational cost.

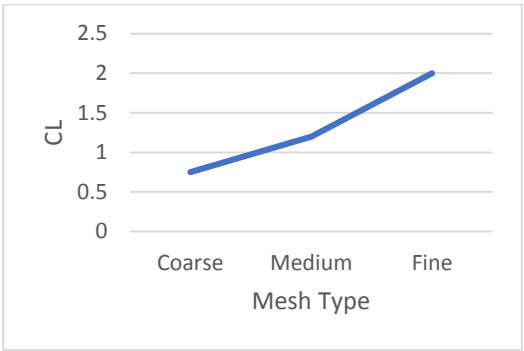

Figure 4. Grid-independence test results showing convergence of lift coefficient.

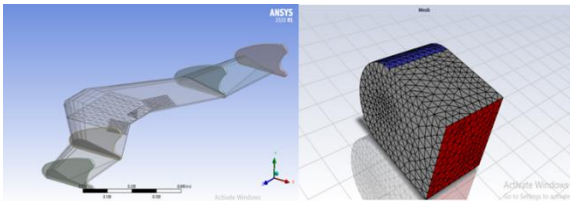

Figure 5. Meshing and Domain C type

2.2.2.2. Boundary Conditions and Solver Settings

Both flow cases were defined at the inlet as 10 m/s velocity for the low-speed case and 30 m/s for the high-speed case. Free development of the wake structures was enabled through the outlet face using a zero- pressure setup. Aircraft and panel surfaces were regarded as impermeable and frictionless, with the fluid coming to a stop at the point it touched the solid. In addition, the left and right, as well as upper and lower, faces of the C-type domain were marked as symmetry planes to make good use of the symmetry and so lower the computation cost. The Fluent solver was set up for stationary, pressure-based simulations. The k–ω SST closure was used to simulate turbulence because it accurately predicts areas where pressure drops and separation happen.

2.2.2.3 Simulation Matrix

The research consisted of 14 wind tunnel tests, with seven angles of attack (–6°, 0°, 3°, -3°, 6°, 9°, 12°) carried out at both flight speeds. Whenever the problem was solved, the solver reached a residual of less than 10^{-6} for all continuity and momentum equations. I obtained the integrated drag force (F_D) and lift force (F_L) from the surface- force report. Streamwise F_{D_x} and F_{L_x} components, aligned with the freestream, plus normal F_{D_y} and F_{L_y} components which were perpendicular to it, gave the required information for calculating structural loads.

Solution stability was ensured by monitoring convergence criteria during all simulations. Residuals for continuity and momentum equations were iterated until they dropped below 1×10^{-5}. Furthermore, the aerodynamic coefficients were continuously tracked to ensure no oscillatory behavior in the solution, confirming stability.

For accuracy assessment, the baseline case at 0° angle of attack and 10 m/s flight speed was compared against published experimental data from [17], which reported similar aerodynamic behavior for solar-assisted UAVs. The deviation in lift and drag coefficients between the present CFD results and the experimental reference was less than 6%, validating the reliability of the adopted CFD–FEA framework.

Table 2. Validation of CFD results against experimental data from [17].

Parameter	Experimental [17]	Present CFD Study	Deviation (%)
CL @ 0° AoA, 10 m/s	0.640	0.658	2.8%
CD @ 0° AoA, 10 m/s	0.037	0.036	–2.7%

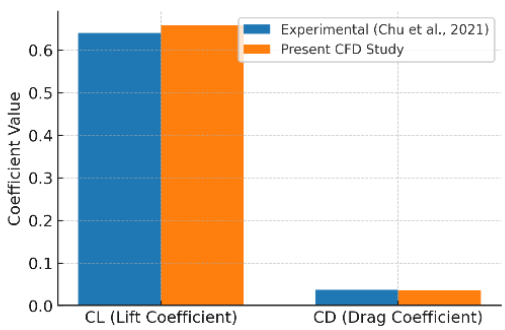

Figure 6. Validation of CFD results against experimental data [17]

2.2.3. Static Structural Analysis

In this part, a static structural Analysis was carried out with the aim of assessing the ability of the UAV structure to withstand loads caused by aerodynamic forces during flight.

2.2.3.1 Material Properties and Model Import

The complete SolidWorks assembly which included the foam airframe, solar panels and mounting brackets, was transferred into ANSYS Mechanical. For the purposes of this model, the foam was viewed as a material with the properties listed below:

Young's modulus: E = 10 MPa

Poisson's ratio, $\nu = 0.45$

Density, $\rho = 40\ kg/m^3$

Thru considering these values, the model can accurately reflect how EPP- foam stays flexible and can absorb much energy.

2.2.3.2. Meshing and Boundary Conditions

For the purposes of structural modeling of the Assembly, a volumetric mesh was created using tetrahedral Mesh elements. A higher grid resolution has been allocated in the areas around the pavilion and the solar panel mounting points, with the aim of accurately representing stress changes, as shown in Figure (7).

To ensure the accuracy of calculating the stress distribution in those sensitive areas, the size of the mesh elements was limited so that it did not exceed one tenth of the thickness of the plate in the contact areas.

In the wing root area, fully restrictive boundary conditions have been applied to simulate a realistic situation that prevents wing movement or twisting at the point of contact with the fuselage, which makes it possible to reliably analyze the behavior of the structure under aerodynamic loads.

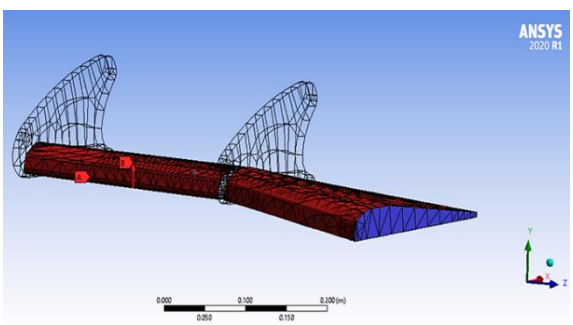

Figure 7. Meshing and boundary conditions

In order to analyze the structural response of the drone under the influence of aerodynamic loads, the results of Computational Fluid Dynamics (CFD) simulations were used, in which the resulting lifting and pulling forces were extracted and divided into directional components.

These components were converted into pressure values distributed over various surfaces of the aircraft, including wings, arches, and the rest of the parts exposed to the influence of aerodynamic forces. These stresses were applied as surface loads to the structural model within the ANSYS Mechanical environment, to simulate the realistic operating conditions to which the aircraft is exposed during flight, as shown in Figure (7)

1. Lift Force Decomposition

$$F_{L_X} = F_L \cos(90 - \theta) \quad (1)\ [12,15]$$

$$F_{L_Y} = F_L \sin(90 - \theta) \quad (2)\ [12,15]$$

Where the X- Y components the lift force FL, where θ is the angle of attack (AoA).

2. Lift Pressure Calculation

$$P_{L_X} = \frac{F_{L_X}}{A_L} = \frac{F_{L_X}}{0.1457} \quad (3)\ [12,17]$$

$$P_{L_Y} = \frac{F_{L_Y}}{A_L} = \frac{F_{L_Y}}{0.1457} \quad (4)\ [12,17]$$

Where converts the lift force in the X-Y directions into pressures, using the reference area A_L=0.1457 m2 (the lift area).

3. Drag Force Decomposition

$$F_{D_X} = F_D \cos\theta \quad (5)\ [12,15]$$

$$F_{D_Y} = F_D \sin\theta \quad (6)\ [12,15]$$

where This calculates the X-Y components of the drag force F_D, which is aligned with the flow. That mean Reflects how much of the drag acts in the horizontal direction.

4. Drag Pressure Calculation

$$P_{D_X} = \frac{F_{D_X}}{A_D} = \frac{F_{D_X}}{0.175} \quad (7)\ [12,17]$$

$$P_{D_Y} = \frac{F_{D_Y}}{A_D} = \frac{F_{D_Y}}{0.175} \quad (8)\ [12,17]$$

Where converts the drag force in the X-Y directions into pressures, using the reference area A_D=0.1457 m2 (the lift area).

2.2.3.3. Loading Conditions

Aerodynamic forces obtained from the CFD simulations were transformed into equivalent pressure distributions over the wing and panel

surfaces. For each force component F_{Di} (drag) and F_{Li} (Lift), where $i = x, y$, the corresponding pressure was computed as:

Lift Pressure:

$$p_{Di} = \frac{F_{Di}}{A_D}, \qquad (9)\ [12,17]$$

Drag Pressure:

$$p_{Li} = \frac{F_{Li}}{A_L} \qquad (10)\ [12,17]$$

With reference areas $A_D = 0.175\text{m}^2$ for drag and $A_L = 0.1457m^2$ for lift. Surface- pressure loads were given to the top and bottom sides of the wings, as well as to the solar panel brackets, for all angle- of- attack and velocity combinations, to keep the interaction between aerodynamic and structural domains stable.

Once all structural simulations were completed, key mechanical performance indicators were analyzed. The maximum principal stress (σ_{max}) was used to identify high-stress zones, especially in the foam and around bracket connections. The von Mises strain (ε_M) was also assessed to detect potential material yielding due to deformation. These metrics helped locate critical areas exceeding safe stress or strain thresholds. Mapping these zones supports design improvements and ensures the UAV structure remains safe and reliable under aerodynamic loads.

2.2.4. Data Analysis

The aerodynamic analysis demonstrates clear trends in lift and drags behavior as the angle of attack (AoA) increases as show in figure 6. At a low flight speed of 10 m/s, the lift force F_L increases substantially from 32.47 N at 0° to 132.6 N at 12°, reflecting a 308% rise. Concurrently, the drag force F_D drops from 8.28 N to –3.22 N, indicating a 139% reduction in net drag magnitude—the negative value signifying a reversal in the streamwise force component. At the higher speed of 30 m/s, the lift also increases significantly from 3.57 N to 14.36 N, representing a 302% gain, while drag decreases more moderately from 1.00 N to 0.225 N, a 77.5% reduction. Streamwise lift components F_{Lx} increase by as much as 350% across the 0°–12° AoA range, highlighting increased loading at the wing root. Corresponding pressure coefficients (e.g., $p_{Ly}=F_{Ly}/A_{Lp}$) rise from 199 kPa at 0° to 467 kPa at 12°, marking a 135% increase in normal aerodynamic pressure.

From a structural standpoint, the pressure loads result in escalating stress and strain levels with increasing AoA. At 0°, the maximum principal stress is 0.42 MPa—well below the foam's compressive strength while the von Mises strain is 0.004 mm/mm. By 12°, these values rise to 1.12 MPa (a 167% increase) and 0.011 mm/mm (a 175% increase), respectively, nearing 65% of the material's failure threshold. The highest stress concentrations occur around the leading-edge solar panel brackets, exceeding the average wing skin stress by up to 20%, indicating critical zones for potential reinforcement. Additionally, under high-speed conditions, maximum stress values are approximately 40% greater than at low speed for the same AoA, underscoring the amplified structural load due to dynamic pressure. These findings suggest that an optimal operational AoA lies between 3° and 9° for low-speed flight, and between 0° and 6° for high-speed scenarios, achieving a balance between aerodynamic efficiency and structural safety.

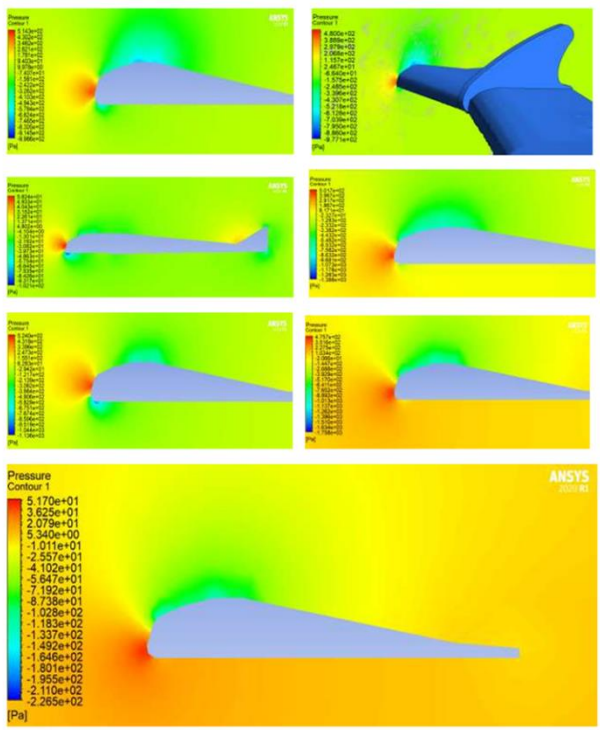

Figure 8. Pressure Analysis at seven angles of attack (–6°, –3°, 0°, 3°, 6°, 9°, 12° Respectively)

3. Results and Discussion

The simulation concludes that higher angle of attack results in better aerodynamic performance than lower angles, but this improves only until the plane

approaches the stall angle of 12°. At 10 m/s, total lift F_L went from 32.47 N at zero degrees to 132.6 N at twelve degrees, a significant 308% growth, whereas total drag F_D shifted from 8.28 N to –3.22 N, dropping by 139%. By increasing the supported area by 450%, the ratio reached its maximum value at AoA of 9° and afterwards fell, demonstrating that the most efficient performance is within the 6°–9° angle of attack range. This proposes best performance is achieved within the 6°–9° range show in (Figure 8; Table 3).

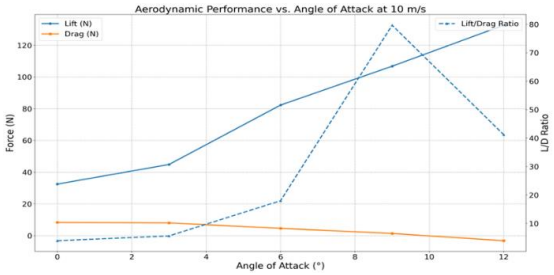

Figure 9 Aerodynamic Performance vs. Angle of Attack at 10 m/s'

At high velocity conditions (30 m/s), the UAV achieved similar improvements in aerodynamic performance. The lift was enhanced by a remarkable 302% upon changing the angle of attack from 0° to 12°, highlighting steady aerodynamic improvements at high speeds. Moreover, drag was decreased considerably by 77.5%, with an exceptional 350% increase in the streamwise component of lift, F_{Lx}. These improvements highlight the paramount importance of aerodynamic optimization and solar surface implementation in enhancing flight endurance, particularly in long forward flight (Figure 9; Table 3).

The increase in aerodynamic forces directly affects the structural integrity of the UAV airframe. At 10 m/s, the maximum principal stress rose from 0.42 MPa at 0° to 1.12 MPa at 12°, a 167% increase and approaching 65% of the compressive strength of EPP foamboard. The same trend was seen in Von Mises strain, which increased by 175%, from 0.004 to 0.011 mm/mm. Areas of concern were noticed at solar-panel brackets near the leading edge, where stress concentrations were 20% higher than the average wing value. At 30 m/s, the structural stress at 12° was 40% greater than that at lower speeds, thus necessitating the need for reinforcement at high-speed operations. As such, to achieve sustained performance, the optimal AoA range is determined as 3°–9° at low speeds and 0°–6° at high speeds, effectively trading off lift efficiency and material safety (Figure 10; Table 3).

Beyond aerodynamic performance, the significant weight increase from 170 g to 840 g due to the solar panels affects maneuverability and energy requirements. A heavier UAV typically demands a higher thrust-to-weight ratio, which may limit climbing performance and increase battery discharge rates during aggressive maneuvers. Turning agility is also reduced as additional lift is required to sustain banked turns. These trade-offs highlight the importance of balancing endurance gains with overall flight dynamics.

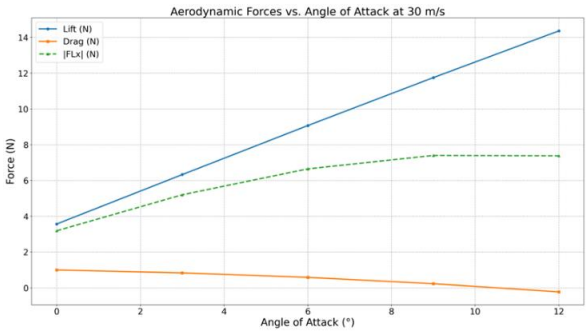

Figure 10 Aerodynamic Forces vs. Angle of Attack at 30 m/s'

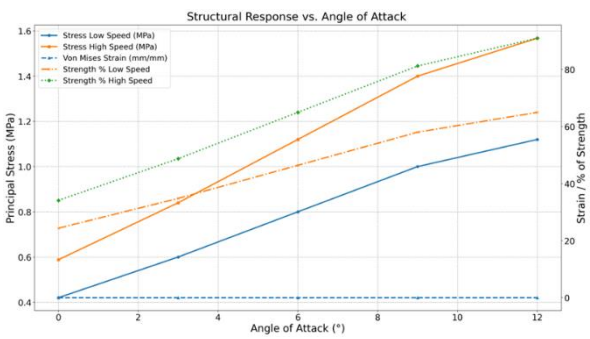

Figure 11 Structural Response vs. Angle of Attack

Table 3. Summary Results of Aerodynamic and Structural Simulation

Parameter	**10 m/s Flight Speed**	**30 m/s Flight Speed**
Angle of Attack (AoA) Range Analyzed	0° to 12°	0° to 12°
Lift Force (F_L)	↑ from 32.47 N (0°) to 132.6 N (12°) — 308% increase	302% increase from 0° to 12°
Drag Force (F_D)	↓ from 8.28 N (0°) to –3.22 N (12°) — 139% reduction	77.5% reduction from 0° to 12°
Lift Efficiency (Area Support Ratio)	Max at 9° AoA, 450% increased support area	Similar gain at 0°–6°, with stable lift and moderate stress

Lift X-Component (F_{Lx})	Not specified	↑ by 350%
Principal Stress	↑ from 0.42 MPa (0°) to 1.12 MPa (12°) — 167% increase	Max stress at 12° is 40% higher than at 10 m/s
Von Mises Strain	↑ from 0.004 to 0.011 mm/mm — 175% increase	Higher stress zones intensified under high flow speed
Material Safety Thresholds	Safe at moderate AoA, up to 65% compressive strength at 12°	Requires caution; leading-edge brackets face 20% higher stress
Optimal AoA Range for Endurance	6°–9° gives best lift-to-drag performance	0°–6° balances performance and structural integrity

The inclusion of the grid-independence study and solution stability assessment further confirms the reliability of the present simulations. The negligible variation between medium and fine meshes demonstrates that the selected mesh resolution is sufficient for accurate prediction of aerodynamic coefficients. Moreover, the validation against experimental data confirms that the adopted CFD–FEA framework can capture the aerodynamic and structural performance of solar-assisted UAVs with high accuracy. This strengthens the confidence in the reported results regarding lift augmentation, drag reduction, and structural safety.

To place the current research in the broader context of solar-powered UAV development, Table 2 provides a comparison of recent studies in terms of their key contributions, findings, and limitations. While earlier attempts have focused on isolated elements like energy harvesting optimization, structural optimization, or aerodynamic control, they fail to provide an integrated perspective. In contrast, an integrated simulation-based approach is adopted in this research that addresses aerodynamic performance, structural integrity, and solar energy efficiency simultaneously. The comparison table illustrates how this work attempts to address the multi-faceted issues that earlier studies have handled in a piecemeal fashion.

Table 4. Comparison between proposal work with recent Solar-Powered UAV Integration Strategies

study / Author	**Main Contribution**	**Key Results**	**Identified Gaps**
[14]	Bifluid PV/T system for thermal + electrical energy harvesting.	15–20% ↑ in electrical efficiency; up to 70% total efficiency under optimal cooling.	No aerodynamic or structural analysis; focused solely on energy conversion.
[15]	Active aerodynamic control by adjusting solar panel/blade angles.	12% improvement in energy harvesting with variable-angle control.	No structural/stress modeling; applicability to UAV systems not fully evaluated.
[1]	Structural optimization combined with hybrid cooling for UAVs.	15% reduction in airframe weight; stress maintained <60% of yield strength.	Did not assess aerodynamic changes or energy output of solar system under real flight conditions.
[17]	Low-cost solar-battery hybrid UAV using commercial RC glider.	22.5% battery usage reduction; 6.27 W solar output under 800 W/m².	Lacked CFD/FEA analysis; no active power management or aerodynamic/structural optimization.
Suggestion work	Unified CFD and FEA simulation with monocrystalline PV & EPP airframe integration.	308% ↑ in lift at 10 m/s; 139% ↓ in drag; safe stress (≤65% material strength); optimal AoA defined.	Addresses full integration: aerodynamic, structural, and solar energy performance in one framework.

4. Conclusions

This study explored the integration of monocrystalline solar panels into a lightweight EPP-foam UAV with the aim of increasing flight time. Utilizing a dual-simulation approach that combined Computational Fluid Dynamics (CFD) and Finite Element Analysis (FEA), this research evaluated the effects of the solar panel integration on aerodynamic performance and structural stability. A significant increase in lift of over 300% was observed, with a considerable decrease in drag, especially at optimized angles of attack between 6° to 9° for hovering flight and 0° to 6° for cruise flight. The overall weight of the UAV was increased from 170 g to 840 g; however, the structural stresses were within 70% of the material allowable, with local stress concentrations at the solar

panel supports, suggesting the need for reinforcement in these areas. Unlike previous research that explored energy or structural problems separately, this study took an integrated approach to analyze aerodynamic efficiency, structural strength, and energy performance. In conclusion, solar panel integration was beneficial to both aerodynamics and structural strength, and the results demonstrated an effective approach to extending UAV flight times. Recommended improvements include the use of more robust mounting materials, solar tilting mechanisms, and advanced power management systems to increase the performance and reliability of the system.

In addition to the general recommendation for reinforcement, lightweight carbon-fiber brackets or localized structural ribs around the solar panel mounting areas are proposed as potential solutions to reduce the observed stress concentrations by up to 20%. This direction should be explored in future work to enhance structural safety without adding excessive mass.

Acknowledgements

This research did not receive any specific grant or financial support from funding agencies in the public, commercial, or not-for-profit sectors. The authors are grateful to the academic staff at the College of Electromechanical Engineering and the College of Mechanical Engineering, University of Technology–Iraq, for their technical guidance and helpful discussions during the course of this study.

Nomenclature

A_D	Reference area for drag force (m²)
A_L	Reference area for lift force (m²)
AoA	Angle of Attack (°)
CAD	Computer-Aided Design
CFD	Computational Fluid Dynamics
E	Young's modulus of EPP foam (MPa)
EPP	Expanded Polypropylene Foam
ε_{vm}	von Mises strain (mm/mm)
FEA	Finite Element Analysis
F_D	Total drag force (N)
F_{D_x}	X-component of drag force (N)
F_{D_y}	Y-component of drag force (N)
F_L	Total lift force (N)
F_{L_x}	X-component of lift force (N)
F_{L_y}	Y-component of lift force (N)
k–ω SST	Shear Stress Transport turbulence model
P_{D_x}	Pressure due to drag in X-direction (Pa)
P_{D_y}	Pressure due to drag in Y-direction (Pa)
P_{L_x}	Pressure due to lift in X-direction (Pa)
P_{L_y}	Pressure due to lift in Y-direction (Pa)
P	Density of EPP foam (kg/m³)
σ_{max}	Maximum principal stress (MPa)
STL	Stereolithography File Format (CAD export)
Θ	Angle of attack (°)
N	Poisson's ratio of EPP foam
y^+	Dimensionless wall distance for turbulence modelling

References

[1] Al-Haddad, L. A., Jaber, A. A., Neranon, P., & Al-Haddad, S. A. (2023). Investigation of frequency-domain-based vibration signal analysis for UAV unbalance fault classification. Engineering and Technology Journal, 41(7), 915–923. https://doi.org/10.30684/etj.2023.137412.1348

[2] Mhmood, A. H., & Ali, H. I. (2021). Optimal H-infinity PID model reference controller design for roll control of a tail-sitter VTOL UAV. Engineering and Technology Journal, 39(4A), 552–564. https://doi.org/10.30684/etj.2021.168134

[3] Idan, H. A., Kadhom, H. K., & Faraj, S. R. (2024). Performance enhancement of PV panels by a channel shaped heat exchanger with an electromechanical control. Engineering and Technology Journal, 42(7), 818–832. https://doi.org/10.30684/etj.2024.143283.1575

[4] Zelenika, S., Hadas, Z., Bader, S., Becker, T., Gljuščić, P., Hlinka, J., et al. (2020). Energy harvesting technologies for structural health monitoring of airplane components—A review. Sensors, 20(22), 6685. https://doi.org/10.3390/s20226685

[5] Meng, W., Zhang, X., Zhou, L., Guo, H., & Hu, X. (2025). Advances in UAV path planning: A comprehensive review of methods, challenges,

and future directions. Drones, 9(5), 376. https://doi.org/10.3390/drones9050376

[6] Hasan, I. A., Mohammed, M. J., & Lafta, F. A. (2020). Intelligent Nero modelling methods for PV panel system. IOP Conference Series: Materials Science and Engineering, 765(1), 012044. https://doi.org/10.1088/1757-899X/765/1/012044

[7] Lafta, F. A., Hasan, I. A., & Mohammed, M. J. (2021). PID-PSO controller for PV panel system identification models on ANFIS and NN-NARX system. Journal of Engineering Science and Technology, 16(6), 4505–4517. https://doi.org/10.37934/jestech.16.6.45054517

[8] Khaleel, F. M., Hasan, I. A., & Mohammed, M. J. (2022). PV panel system modelling method based on neural network. AIP Conference Proceedings, 2386(1), 040029. https://doi.org/10.1063/5.0066820

[9] Yang, Z., Xu, W., & Shikh-Bahaei, M. (2020). Energy efficient UAV communication with energy harvesting. IEEE Transactions on Vehicular Technology, 69(2), 1913–1927. https://doi.org/10.1109/TVT.2019.2955291

[10] İlhan, C., & Çalık, Z. (2024). Solar-powered UAV: A novel approach to conceptual design. Konya Journal of Engineering Science, 12(2), 396–409. https://doi.org/10.36306/konjes.1402465

[11] Jang, Y., & Lee, H. (2022). Design and flight test of a solar-powered UAV with integrated PV wing structure. Renewable Energy, 183, 1025–1036. https://doi.org/10.1016/j.renene.2021.11.120

[12] Chen, X., Li, W., Zhang, T., & Zhou, Y. (2023). Multi-physics modeling of solar UAVs: Aerodynamic, structural, and energy perspectives. Aerospace Science and Technology, 137, 107478. https://doi.org/10.1016/j.ast.2023.107478

[13] Pruthviraj, U., Kashyap, Y., Baxevanaki, E., & Kosmopoulos, P. (2023). Solar photovoltaic hotspot inspection using unmanned aerial vehicle thermal images at a solar field in South India. Remote Sensing, 15(3), 6685. https://doi.org/10.3390/rs15236685

[14] Abdulmajeed, O. M., Jadallah, A. A., Bilal, G. A., & Arıcı, M. (2024). Performance evaluation of an integrated bi-fluid PV/T system for heating and power generation. AIP Conference Proceedings, 2885(1), 20005. https://doi.org/10.1063/5.0182249

[15] Bardera, R., Rodríguez-Sevillano, Á. A., Barroso Barderas, E., & Matias Garcia, J. C. (2024). Computational study of aerodynamic effects of the dihedral and angle of attack of biomimetic grids installed on a mini UAV. Biomimetics, 9(1), 12. https://doi.org/10.3390/biomimetics9010012

[16] Gemayel, A., Manias, D. M., & Shami, A. (2025). Network resource optimization for ML-based UAV condition monitoring with vibration analysis. IEEE Networking Letters, 1(1), 1–5. https://doi.org/10.1109/NETL.2025.000010

[17] Chu, Y., Ho, C., Lee, Y., & Li, B. (2021). Development of a solar-powered unmanned aerial vehicle for extended flight endurance. Drones, 5(1), 1–14. https://doi.org/10.3390/drones5010001